Acta Materialia 306 (2026) 121878

Contents lists available at ScienceDirect

Acta Materialia

journal homepage: www.elsevier.com/locate/actamat

Full length article

Double-tough and ultra-strong ceramics: Leveraging multiscale toughening mechanisms through Bayesian optimization

Francesco Aiello [a], Jian Zhang [a], Johannes C. Brouwer [b], Michele Cassetta [c,d], Mauro Salazar [a,*], Diletta Giuntini [a,e,**]

[a] Department of Mechanical Engineering, Eindhoven University of Technology, P.O. Box 513, Eindhoven, 5600 MB, The Netherlands
[b] Department of Materials Science and Engineering, Delft University of Technology, Mekelweg 2, Delft, 2628 CD, The Netherlands
[c] Department of Earth Science, University of Torino, Torino, 10125, Italy
[d] Department of Engineering for Innovation Medicine, University of Verona, Verona, 37134, Italy
[e] Institute of Advanced Ceramics, Hamburg University of Technology, Denickestrasse 15, Hamburg, 21073, Germany

ARTICLE INFO

Keywords:
Ceramic material
Bio-inspired materials
Phase transformation
Strengthening mechanism
Microstructure design

ABSTRACT

An optimization-driven approach is presented to create a "double-tough" ceramic. The material features two main toughening mechanisms – crack deflection in a brick-and-mortar microstructure, and transformation toughening in the mortar – and it is engineered to achieve high strength and fracture toughness levels simultaneously. The material design involves high-strength alumina bricks interconnected via a ceria-stabilized zirconia mortar. Given that the design of the optimal material, featuring multiscale toughening mechanisms, typically requires a laborious trial-and-error approach, a Bayesian optimization framework is proposed to streamline and accelerate the experimental campaign. A Gaussian process is used to emulate the material's mechanical response, and a cost-aware batch Bayesian optimization is implemented to efficiently identify optimal design process parameters, accounting for the cost of experimentally varying them. This approach expedites the optimization of the material's mechanical properties. As a result, a bio-inspired all-ceramic composite is developed, exhibiting an exceptional balance between bending strength (704 MPa) and fracture toughness (13.6 MPa $m^{0.5}$), along with a stress intensity factor at crack initiation of 6.7 MPa $m^{0.5}$. The material exhibits significantly higher strength than both nacre-like ceramic composites and transformation-toughened zirconia at comparable toughness levels.

1. Introduction

Ceramic materials are renowned for their exceptional hardness and strength, coupled with high-temperature and chemical stability. However, their inherent brittleness presents significant challenges, limiting their broad applicability [1]. Balancing strength and toughness is a common challenge in materials science, as they are two crucial yet conflicting properties [2]. A well-established solution relies on the phase transformation toughening featured by zirconia, whilst more recently bio-inspired nacre-like structures have started to prove effective in leading to tough ceramic-based composites [3–12].

Nacre-like composites mimic the hierarchical structure of natural nacre, known for its exceptional combination of strength and toughness [13] through mechanisms such as crack deflection enabled by a "brick-and-mortar" microstructure [14–20]. Aluminum oxide (Al_2O_3) monocrystalline platelets, known for their high strength [21,22], are commonly used in these structures [23–27]. A relatively ductile mortar phase is, in turn, critical for crack deflection, stress distribution, and energy dissipation [28,29]. In this context, ceramic mortars, such as silica, calcia, or aluminum borate, can further enhance toughness and strength while maintaining high temperature and corrosion resistance [30–32].

Zirconia (ZrO_2) emerges here as a promising candidate for the "mortar" phase due to its higher compliance compared to alumina [33] and its toughening capability from stress-induced phase transformations [4], which leads to a quasi-ductile behavior. The use of zirconia in nacre-like aluminas has been explored in previous studies via the addition of zirconia particles in the mortar, confirming the importance of having the zirconia particles in their tetragonal phase [34] to achieve improvements in the fracture toughness [35]. Balancing the grain size of tetragonal zirconia is essential: too large causes spontaneous

* Corresponding author.
** Corresponding author at: Department of Mechanical Engineering, Eindhoven University of Technology, P.O. Box 513, Eindhoven, 5600 MB, The Netherlands.
E-mail addresses: m.r.u.salazar@tue.nl (M. Salazar), d.giuntini@tue.nl (D. Giuntini).

https://doi.org/10.1016/j.actamat.2025.121878
Received 21 June 2025; Received in revised form 28 November 2025; Accepted 28 December 2025
Available online 13 January 2026

transformation, while too small stabilizes the tetragonal phase, preventing transformation even under high stress [36]. This balance can be achieved by introducing stabilizing oxides, or controlling grain size [4].

If then one wants to develop new nacre-like ceramics with a zirconia mortar, an optimal balance needs to be identified for the mortar thickness to enable transformation toughening at useful stress levels, without compromising on strength. Additionally, a set of processing parameters needs to be identified to yield the target micro- and nano-structures.

Traditional material optimization relies on trial-and-error experimentation, which is time-consuming and overlooks complex variable interactions. Bayesian Optimization (BO) is a technique specifically tailored to optimize objectives that are computationally expensive and subject to noisy values, lack a straightforward analytical formulation, and present challenges in efficiently determining gradients [37]. BO can thus reduce the number of evaluations needed to discover optimal solutions [38]. Recently, BO explored the optimal balance between strength, toughness, and specific volume within a numeric finite element model of a nacre-inspired composite [39], investigating a mortar with compliance one to three orders of magnitude higher than that of the bricks, consistent with a polymer–ceramic nacre-inspired composite.

In this work, we leverage BO to guide the fabrication of an all-ceramic composite that exploits two primary toughening mechanisms: crack deflection, through a brick-and-mortar microstructure, and crack shielding, via transformation toughening within the zirconia mortar, yielding a "double-tough" ceramic composite. The crack deflection mechanism operates at the microscale (the scale of the bricks), the crack shielding at the nanoscale (in the sub-μm-thick mortar). The authors have previously demonstrated, via a computational design framework [40], that coupling nanoscale and microscale toughening mechanisms in brick-and-mortar ceramic materials featuring stress-induced phase transformation within the mortar leads to a significant improvement in fracture performance. There are, however, several challenges in developing such a double-tough ceramic: (1) The phase transformation in zirconia requires a minimum grain size to operate at realistic stresses, whilst nacre-mimetics typically need ultrathin mortars; (2) the parameter space to explore, in terms of material composition, microstructure and process parameters, is extremely broad. To overcome these challenges and achieve the goal of maximizing both strength and toughness, we employ Bayesian optimization methods to expedite the experimental campaign. The result is an all-ceramic composite material featuring a "brick-and-mortar" microstructure, where alumina "bricks" are interconnected through a zirconia "mortar" that can undergo a phase transformation.

The paper is organized as follows. Section 2 introduces the meta-experimental optimization methodology employed to guide the design of the double-tough ceramics. Section 3 details the materials, processing steps, and characterization techniques. Section 4 presents the results and discussion, beginning with the pre-optimization processing, followed by the outcomes of the material optimization, and examining the influence of processing parameters on phase composition, microstructure, density, and mechanical properties. Finally, Section 5 summarizes the main conclusions and highlights the key contributions of this work.

2. Meta-experimental optimization methodology

By meta-experimental optimization, we refer to a systematic approach that optimizes how each experiment is designed and iterated to make the entire experimental campaign more efficient. Fig. 1 depicts the schematic diagram illustrating the various steps involved in the design and optimization of our all-ceramic "double-tough" composite material.

We fabricate the material by coating commercial Al_2O_3 platelets with ceria-stabilized zirconia via a sol–gel and calcination process, and sintering the resulting powder using spark plasma sintering, achieving a sub-micron zirconia layer that serves as the mortar phase in the "brick-and-mortar" composites. We choose ceria to stabilize the zirconia in its tetragonal phase thanks to its high flaw tolerance [41–43], and low-temperature degradation resistance [44,45]. The materials are then characterized for their composition, microstructure and mechanical properties. The manufacturing and characterization steps are described in detail in the next section (Materials and Methods).

For the material design, numerous process parameters, such as calcination and sintering temperatures, pH, mortar quantity, and platelet aspect ratio, need consideration, making exhaustive testing impractical. To address this, we first narrow the parameter space by focusing on those with the most significant impact on mechanical properties: ceria mole fraction (x_{CeO_2}), mortar mass ratio (X_m), and dwell temperature (T_{dwell}). The amount of mortar affects stress redistribution and defect tolerance [46], the ceria content influences phase transformation and toughening [36,47], and the dwell temperature impacts material densification and grain growth [48].

We use BO to guide the selection of experimental conditions in a systematic way. We define an objective function $f(\mathbf{x})$ as a combination of normalized flexural strength and stress intensity factor at the limit, which BO then aims to maximize. Unlike traditional methods, BO uses a surrogate model and an acquisition strategy to determine the subsequent experiment based on prior data.

The surrogate model is here based on a Gaussian Process (GP). A GP acts as an approximate model of the objective function $f(\mathbf{x})$. It learns from the experiments already performed and predicts both the expected value of the function and the uncertainty at any untested point. These predictions are then used by the acquisition function to guide the next experiment. To initialize the BO, we train the GP by selecting an initial set of process parameters based on literature observations. These data is used solely to define the search domain, and no measured strength or toughness data is employed to influence the optimization outcome. The data selection criteria are based on excluding parameter regions known to lead to undesired material behavior. Specifically, the mortar content in natural nacre typically ranges around 5 vol% [15], while in brick-and-mortar-like materials, it can increase significantly, reaching up to 45 vol% [46,49]. In zirconia-toughened alumina, the zirconia content is generally kept below 30 wt.% [50–53] due to challenges in maintaining dispersed zirconia grains in the tetragonal phase above 16 vol% [50,54]. Ceria serves as a stabilizing agent for tetragonal zirconia at room temperature [55]. The solubility limit of the tetragonal solid solution is around 18 mol% ceria at 1400 °C, decreasing to 16 mol% at 1200 °C [56]. Typically, ceria content in ceria-stabilized zirconia is less than 12 mol% [57–63]. Higher ceria concentrations result in the formation of a stable cubic zirconia phase [55,56,63]. The stability of tetragonal zirconia depends on grain size [47], leading to the concept of critical size for spontaneous transformation to the monoclinic phase. Dwell temperature selection is crucial to achieve final density without excessive grain growth or induced monoclinic transformation during sintering [55,64].

In BO, the acquisition function determines which experiment to perform next by using the surrogate model's predictions. It balances exploration, which focuses on sampling regions of the design space where the objective function is uncertain, and exploitation, which focuses on sampling regions that are likely to yield high objective values. In our work, we adopt a sequential batch algorithm introduced by González et al. [65] to select multiple points simultaneously. We further modify the acquisition strategy to account for experimental cost, preferring points that require minimal additional material processing steps. Additional details on the BO are provided in the following section and in the Supplementary Materials.

3. Materials and methods

This section describes the process designed to create nacre-like alumina with a compliant phase of ceria-stabilized zirconia. We then elaborate on the methodologies used for microstructural and mechanical characterization, along with the procedure employed to optimize the mechanical properties.

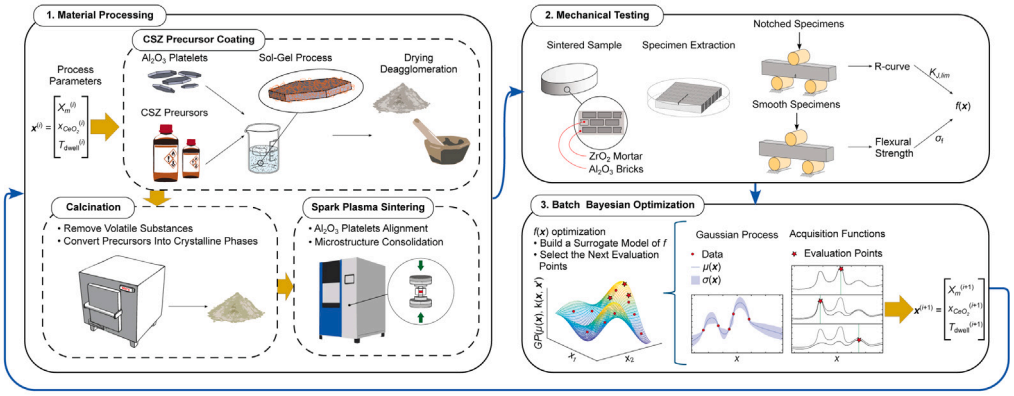

Fig. 1. Schematic diagram of material design via Bayesian Optimization (BO). The material consists of Al_2O_3 platelets coated by ceria-doped zirconia, which are consolidated in brick-and-mortar ceramic composites via spark plasma sintering. The process parameters for which we optimize are the amount of zirconia mortar (X_m), the amount of ceria doping in the zirconia (x_{CeO_2}) and the spark plasma sintering dwell temperature (T_{dwell}). Each sample is tested for flexural strength and fracture toughness. The processing and testing of each ceramic composite is followed by a BO step, which guides the next experimental iteration. CSZ indicates ceria-stabilized zirconia, GP indicates the Gaussian Process used in the BO.

3.1. Materials

To fabricate the "brick" phase, we used commercial Al_2O_3 platelets (Serath YFA10030BJ) supplied by Kinsei Matek Co., Ltd. (Osaka, Japan), featuring an average particle size of 10 μm with fine particles removed, and an aspect ratio ranging from 25 to 30. For the creation of the "mortar" phase, we employed the following materials: a 70 wt.% solution of zirconium(IV) propoxide, $Zr(OC_3H_7)_4$, in 1-propanol (with a density of 1.044 g cm^{-3} at 25 °C), cerium(III) nitrate hexahydrate, $Ce(NO_3)_3 \cdot 6H_2O$, of 99% trace metals basis, and nitric acid, HNO_3, with a concentration exceeding 65%. These materials were sourced from Merck KGaA (Darmstadt, Germany).

3.2. Processing of the bulk double-tough ceramics

We made the material by coating with ceria-stabilized zirconia. Subsequently, we spark plasma sintered the resulting powder to obtain fully dense bulk materials with the desired microstructure. For the coating procedure, we used sol–gel methods, following a methodology based on the one outlined in [66,67].

We prepared a water solution of ceria-stabilized zirconia precursors for the coating step. For each liter of water, we added 71.57 ml of $Zr(OC_3H_7)_4$ reagent (denoted as $V_{Zr(reag.)}$), 30 ml of HNO_3 reagent, and a mass, $m_{Ce(reag.)}$, of $Ce(NO_3)_3 \cdot 6H_2O$ reagent. We achieved different ceria mole fractions, x_{CeO_2}, in the coating by adjusting $m_{Ce(reag.)}$. We determined $m_{Ce(reag.)}$ through stoichiometric calculations using

$$m_{Ce(reag.)} = n_{Ce} \frac{100}{p_{Ce(reag.)}} M_{Ce(NO_3)_3 \cdot 6H_2O}, \tag{1}$$

with

$$n_{Ce} = \frac{x_{CeO_2}}{1 - x_{CeO_2}} n_{Zr}, \tag{2}$$

$$n_{Zr} = V_{Zr(reag.)} \frac{c_{Zr(reag.)}}{100} \frac{\rho_{Zr(reag.)}}{M_{Zr(OC_3H_7)_4}}, \tag{3}$$

where n represents the amount of the element in solution (in mol), M the molar mass, p the reagent purity, c the reagent weight concentration, and ρ the mass density; each symbol refers to its subscripts. Upon the introduction of the $Zr(OC_3H_7)_4$ reagent, the mixture underwent hydrolysis, leading to the formation of an initially opaque mixture. We subjected this mixture to stirring at room temperature on a magnetic stirrer at 500 rpm for a duration of 24 hours, resulting in the solution becoming transparent.

After preparing the coating solution, we coated the Al_2O_3 platelets. Initially, we added 10 g of Al_2O_3 platelets to 180 ml of distilled water, followed by a 15-minute sonication process. Subsequently, we introduced a quantity of the coating solution to achieve the final "mortar" mass ratio, X_m defined as

$$X_m = \frac{m_m}{m_{Al_2O_3} + m_m}, \tag{4}$$

with m_m is the "mortar" mass, and $m_{Al_2O_3}$ the alumina platelets mass ("bricks"). We calculated the coating solution volume to add under the assumption that all the added zirconium and cerium would undergo complete oxidation during calcination. Given the molarity of zirconium in the prepared coating solution (approximately 0.16 mol L^{-1}), we selected a volume of coating solution containing the required moles of Zr, n_{Zr}, determined by

$$n_{Zr} = (1 - x_{CeO_2}) \frac{\frac{X_m}{1-X_m} m_{Al_2O_3}}{(1 - x_{CeO_2}) M_{ZrO_2} + x_{CeO_2} M_{CeO_2}}. \tag{5}$$

After adding the coating solution, we mixed it on a hot plate at a temperature of 70 °C for 5 h, followed by an additional 19 h at room temperature. Subsequently, we dried the solution and deagglomerated the coated platelets using a mortar and pestle.

We subjected the obtained powder to calcination in a muffle furnace at 600 °C for 4 h in an air environment. This process served the dual purpose of removing volatile substances and oxidizing the elements in the "mortar" phase.

For the subsequent sintering process, we used 3.5 g samples of the calcined powder and employed the spark plasma sintering technique [68,69]. The samples were placed within 20 mm diameter graphite dies. Additionally, a 0.3 mm graphite sheet was placed onto the side surface of the die, and two circular sheets were inserted between the sample and the die bases. The sintering operation was conducted under vacuum conditions. The applied sintering cycle involved a constant heating rate of 125 °C min^{-1} until reaching the maximum temperature, denoted as T_{dwell}. Subsequently, we maintained this constant temperature for 10 min, followed by a controlled cooling phase with a rate of 16 °C min^{-1}. Throughout the ramp-up to the maximum temperature, we maintained a pressure of 16 MPa. During the temperature hold period, we increased the pressure to 80 MPa. To prevent the formation of cracks in the material and safeguard the equipment, we then reduced the pressure to 50 MPa during the cooling phase (see also Supplementary Material, Figure S1).

We determined the final mass density of the sintered sample, ρ_s, using Archimedes method. We measured the sample's mass both in air, m_a, and when immersed in water, m_w. In our calculations, we neglected the buoyancy of the sample in air. We calculated ρ_s using [70]

$$\rho_s = \frac{m_a}{m_a - m_w} \rho_w, \tag{6}$$

with $\rho_w = 0.998\,g\,cm^{-3}$ denoting the mass density of water at a temperature of 20 °C and a pressure of 1 atm [71]. We calculated the final relative density of the sample, ρ_r, by dividing ρ_s by the theoretical density, ρ_t, obtained from the rule of mixture [72]

$$\frac{1}{\rho_t} = \sum_i \frac{\chi_i}{\rho_i}, \tag{7}$$

where χ_i is the weight fraction of the ith phase and ρ_i its mass density. The mass densities of α-Al_2O_3, t-ZrO_2, and m-ZrO_2 were taken as 3.965, 6.10, and $5.83\,g\,cm^{-3}$, respectively [73,74].

We estimated the mortar volume fraction, v_m, in terms of the mortar mass fraction using [75]

$$v_m = \frac{X_m/\rho_m}{X_m/\rho_m + (1 - X_m)/\rho_b} \tag{8}$$

where ρ_m is the average mortar density, equal to $5.97\,g/cm^3$, calculated as the arithmetic mean of tetragonal and monoclinic zirconia densities [74], and ρ_b is the density of α-Al_2O_3, equal to $3.965\,g/cm^3$ [73].

3.3. Micrographic analysis

We conducted micrographic analyses employing a scanning electron microscope (SEM) equipped with an energy dispersion X-ray analyzer (EDX) to assess the effectiveness of platelet coating, examine the final material microstructure, and inspect the fracture surfaces of tested specimens. We use low vacuum imaging at a chamber pressure of 0.6 mbar to reduce charging, with a working distance of 5 mm, beam voltage ranging between 5 and 10 kV, and a spot size between 2.5 and 3.

For sample preparation, we embedded a portion of the material in a 30 mm diameter capsule using the thermosetting bakelite resin with carbon filler PolyFast supplied by Struers. Subsequently, we conducted automated grinding using abrasive papers with grit sizes ranging from 320 to 4000 grit, gradually increasing grinding times. During this process, we used water as a cooling fluid, applied a force of 35 N to each specimen, and maintained a polishing head speed of 300 rpm, rotating in the same direction as the polishing platen. Following grinding, we polished the samples using a 1 µm diamond suspension. For this operation, we reduced the rotation speed of the platen and head by half.

Furthermore, we subjected polished samples to thermal etching. This process entailed removing them from the mounting resin and placing them in a furnace set at a temperature 150 °C lower than T_{dwell}, with an etching duration of 30 minutes [76].

3.4. X-ray diffraction analysis

We conducted an X-ray diffraction (XRD) analysis using a Bruker D2 PHASER XE-T instrument equipped with a Co-anode X-ray source. We analyzed the material at various stages of the process, including before and after calcination, as well as after sintering. The XRD measurements covered a range of diffraction angles, 2θ, from 25 to 55 degrees. We collected data points at an increment of 0.01 degrees, with a time step of 1 second per step.

We used GSAS II software [77] for the data analysis. We initiated a crystal structure refinement process with the crystal structure models of tetragonal zirconia [78], monoclinic zirconia [79], and alpha alumina [80] sourced from the Crystallography Open Database [81]. We performed parameter refinement for the phase quantities, sample displacement, lattice parameters, and crystallite size. To account for preferred orientation effects in crystallites, we applied a spherical harmonics model of order 2.

3.5. Raman spectroscopy

We obtained Raman spectra using a Thermo Scientific DXR2 (Madison, WI, USA), which features switchable solid-state lasers operating at an excitation wavelength (λ_{exc}) of 532 nm. To suppress the Rayleigh line, we employed an edge filter. We dispersed the scattered light using a custom grating and recorded it with a thermoelectrically cooled charge-coupled device. The grating we used (2400 lines/mm) enabled measurements in the spectral range of 30 to $1800\,cm^{-1}$, achieving a resolution of approximately $3\,cm^{-1}$.

We conducted depth profiling by measuring Raman scattering along the Z-axis of the sample stage. Starting at the top of the fracture surface, we took measurements inward in steps of approximately 4 µm. We maintained the laser power at the sample surface at 10 mW and focused it onto a spot about 1 µm in diameter using a 100× objective lens. We adjusted the integration time and the number of accumulations based on the distance from the surface.

3.6. Mechanical characterization

We conducted flexural strength and crack growth resistance characterizations of the sintered material at room temperature using three-point bending tests under displacement control on both smooth and notched specimens. The flexural strength, σ_f, was determined from tests on smooth specimens, following the ISO14704:2016 standard [82]. The material's crack growth resistance curve (R-curve) was derived from tests on notched specimens.

From the R-curve, we calculated two key parameters: the stress intensity factor at crack initiation, denoted as $K_{J,0}$ (corresponding to a crack extension, Δa, of 0), and the stress intensity factor at the crack extension limit, denoted as $K_{J,lim}$, in accordance with ISO12135:2021 [83], corresponding to $\Delta a = 0.25(W - a_0)$.

Additional details of the procedure are provided in the Supplementary Material.

3.7. Material optimization

Our approach focuses on maximizing the objective function $f(\mathbf{x})$, where $\mathbf{x} = [x_{CeO_2}, X_m, T_{dwell}]$. We defined the function $f : \mathcal{X} \to \mathbb{R}$, where $\mathcal{X} \subseteq \mathbb{R}^d$, as a linear combination of dimensionless mechanical properties $K_{J,lim}/\bar{K}_{J,lim}$ and $\sigma_f/\bar{\sigma}_f$, with $\bar{K}_{J,lim}$, and $\bar{\sigma}_f$ representing reference properties. These reference properties are chosen from similar types of existing materials to normalize the obtained mechanical properties. We used the stress intensity factor at crack limit extension to fully exploit the toughening phenomena that occur during crack propagation. The optimization problem can be summarized as

$$\max_{\mathbf{x}\in\mathcal{X}} f(\mathbf{x}) = \max_{\mathbf{x}\in\mathcal{X}} \left[\lambda \frac{K_{J,lim}(\mathbf{x})}{\bar{K}_{J,lim}} + (1 - \lambda) \frac{\sigma_f(\mathbf{x})}{\bar{\sigma}_f} \right]. \tag{9}$$

where λ is a weight parameter.

We addressed this problem using BO. Unlike traditional Design of Experiments methods with fixed experiment numbers and limited adaptability, BO follows a sequential approach [84]. It uses a surrogate model of the actual system and a strategy to decide on the next experiment based on existing data. This helps balance between exploring new areas and exploiting known information [37]. The surrogate model is based on a Gaussian process, which approximates the objective function $f(\mathbf{x})$ and provides predictions of both its expected value and associated uncertainty:

$$f(\mathbf{x}) \sim \mathcal{GP}(\mu(\mathbf{x}), k(\mathbf{x}, \mathbf{x}')), \tag{10}$$

where $\mu(\mathbf{x})$ and $k(\mathbf{x}, \mathbf{x}')$ represent the mean function and the covariance function of $f(\mathbf{x})$. To select the next experimental points, we use an acquisition function based on expected improvement per unit cost (EI_{pu}). To generate multiple candidates in a single iteration, we employ a sequential batch algorithm with local penalizers ϕ that account for

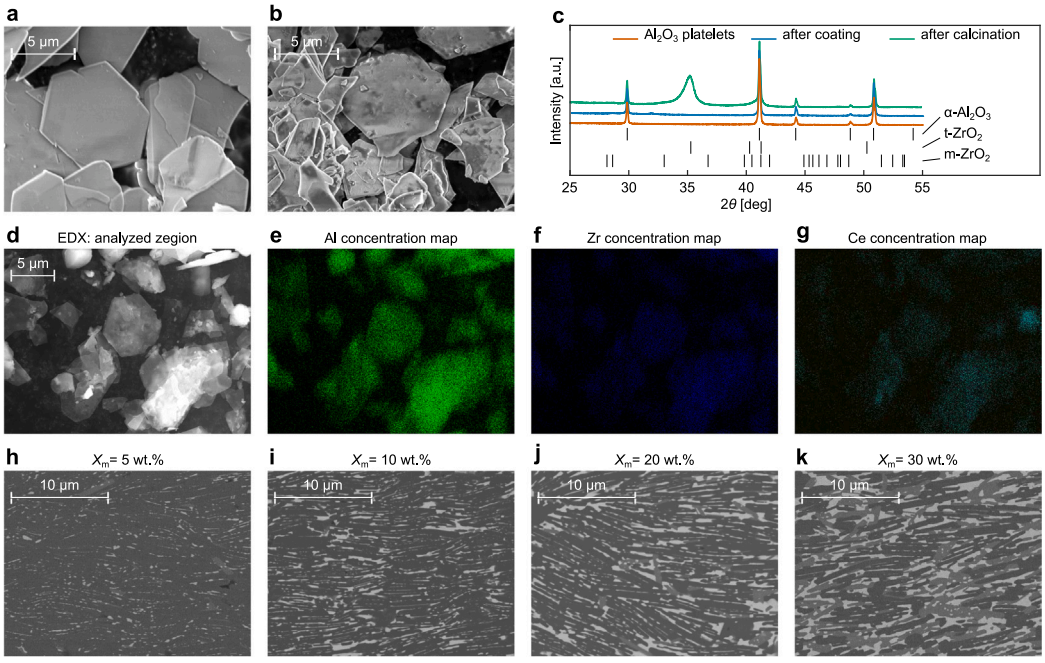

Fig. 2. Material Design: (a, b) SEM images of alumina platelets before and after being coated with 10 wt.% ceria-doped zirconia mortar, showing effective material coverage. (c) XRD spectra of Al_2O_3 platelets, right after being coated with 30 wt.% mortar and 12 mol% ceria, and after being calcined, revealing a fully tetragonal zirconia coating. Theoretical diffraction peaks for alpha alumina (α-Al_2O_3), tetragonal zirconia (t-ZrO_2), and monoclinic zirconia (m-ZrO_2) are shown. (d–g) SEM images with EDX analysis of alumina platelets coated with 20 wt.% zirconia stabilized with 6 mol% ceria, showcasing elemental concentration with homogeneous distribution. (h–k) SEM images of material microstructures with varying mortar content (5-30 wt.%, equivalent to ~ 3.2-22 vol%), with zirconia as the light phase and alumina as the dark phase. The microstructures reveal the alignment of alumina platelets in a preferential direction, with the mortar becoming continuous and more uniform as its content increases. SEM images were taken under high vacuum with a beam voltage of 10 kV (d–g) and 5 kV (a, b, h–k); micrographs (h–k) using a back-scattered electron detector in a plane aligned with the sintering direction.

previously selected points within the same batch [65]. Each kth batch point $\mathbf{x}_k^b$ is calculated as:

$$\mathbf{x}_k^b = \arg\max \left[\mathrm{EI}_{\mathrm{pu}}(\mathbf{x}, \mathcal{I}_n) \prod_{i=1}^{k-1} \phi(\mathbf{x}; \mathbf{x}_i^b) \right], \tag{11}$$

where $\mathcal{I}_n$ represents the available data set. During optimization, the values for ceria concentration, mortar content, and dwell temperature were rounded to the nearest multiples of 1 mol%, 1 wt.%, and 50 °C, respectively. Additional details on the surrogate model and acquisition strategy are provided in the Supplementary Material.

4. Results and discussion

4.1. Pre-optimization material processing: platelet coating and brick-and-mortar microstructures

Coating the Al_2O_3 platelets with ZrO_2 mortar. In the pre-optimization phase, we analyzed the coating uniformity and the zirconia phases present in the prepared powder. Fig. 2 (a, b) presents comparative SEM images of alumina platelets in their as-received state (Fig. 2(a)) and after undergoing the coating and deagglomeration process (Fig. 2(b)), before the subsequent calcination. Fig. 2(b) illustrates representative coated platelets, demonstrating qualitative evidence of material coverage without observable agglomerations.

Fig. 2(c) depicts XRD spectra obtained from alumina platelets in their as-received state, after coating (pre-calcination), and immediately after calcination. The as-received platelets exhibited peaks corresponding to the theoretical peaks of α-Al_2O_3. Post-coating, no other crystalline phases were evident, as indicated by the absence of additional peaks in the spectrum. Upon calcination, a crystalline phase emerged, notably characterized by a peak at around 35 degrees, corresponding to the diffraction peak of t-ZrO_2. No peaks indicative of m-ZrO_2 were observed in the spectrum. After refinement, we determined the crystallite size of tetragonal zirconia to be 13 nm, consistent with the grain size of the zirconia coating obtained using a similar method [66].

We conducted EDX analysis on the coated platelets after calcination to assess the uniformity of elements. Fig. 2(d) displays a SEM image of alumina platelets coated with 20 wt.% of mortar and 6 mol% of ceria, with corresponding aluminum, zirconium, and cerium maps shown in Fig. 2 (e–g). The elements exhibit homogeneous distribution. The low intensity of the cerium element map is attributed to its content, constituting 6 mol% of the mortar phase, which, in turn, represents 20 wt.% of the material. A detailed elemental scan reveals a zirconium-to-cerium ratio of 9.45: 0.65, consistent with the theoretical 6 mol% present in the analyzed coating.

The microstructures resulting from sintering are depicted in Fig. 2 (h–k) for varying amounts of mortar, ranging from 5 wt.% (~ 3.2 vol%) to 30 wt.% (~ 22 vol%). We captured the images along a plane aligned with the direction of load application during sintering, oriented vertically in the figures. We used back-scattered electron detector imaging to emphasize the contrast between the "brick" and "mortar" phases, corresponding to the dark and light phases, respectively, due to the distinct atomic numbers of Al and Zr [85].

Brick-and-mortar microstructure. The microstructures reveal the alignment of alumina platelets in a preferential direction. The orientation, orthogonal to the midplane (parallel to the crystallographic c-axis), is aligned parallel to the direction of the applied load during sintering. Fig. 2(h), shows the mortar phase discontinuously distributed around the platelets, with absence between some platelets and small agglomerates observed on the sides of the alumina platelets. As the mortar content increases, the thickness of the mortar phase becomes more continuous and uniform, as depicted in Fig. 2 (i–k).

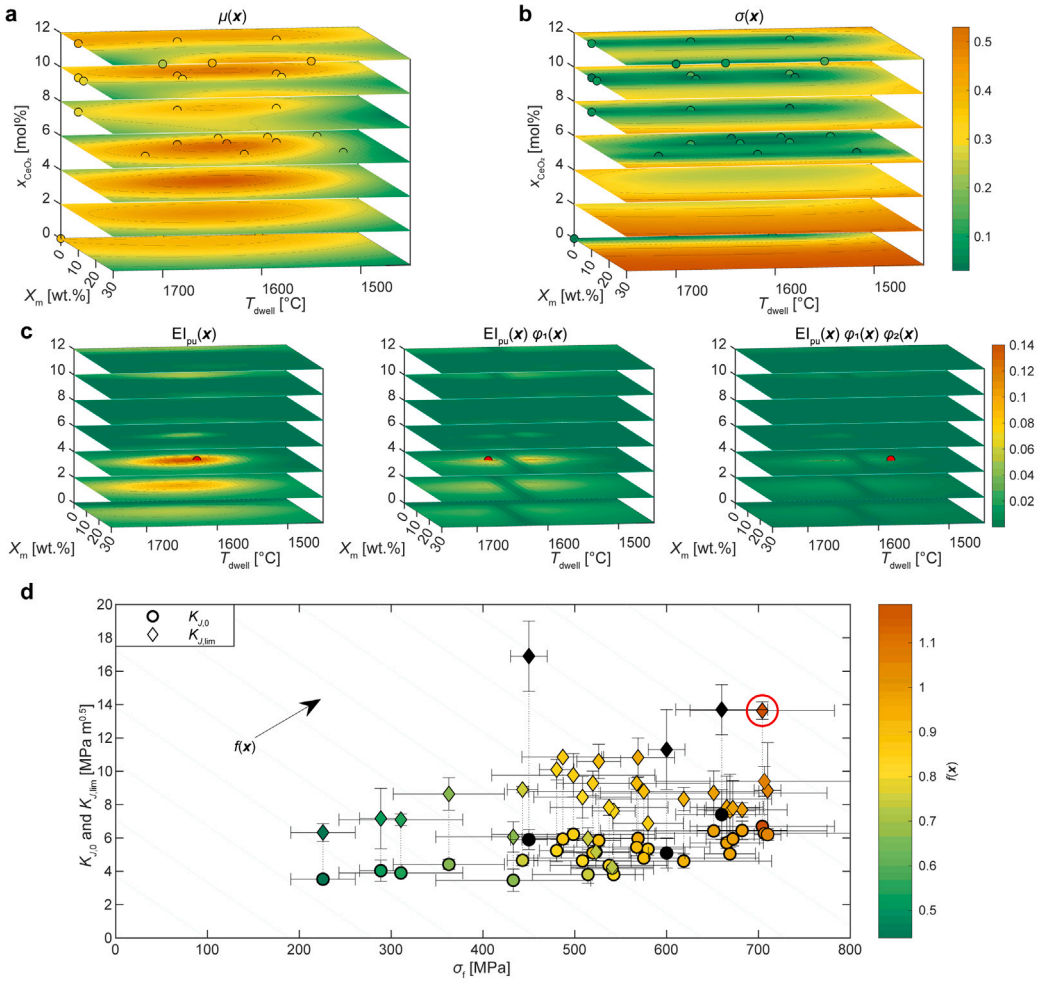

Fig. 3. Optimization Process. (a) Posterior mean $\mu(\mathbf{x})$ and (b) posterior standard deviation $\sigma(\mathbf{x})$ of the objective function $f(\mathbf{x})$, along with the training dataset. (c) Acquisition functions across three iterations, showing batch point selection (red dots) for exploration, represented by the maximum point, where the coordinates correspond to the optimal process parameters. Functions are expressed in terms of mortar content X_m, dwell temperature T_{dwell}, and ceria mole fraction x_{CeO_2}, visualized through contour plots at constant x_{CeO_2}. In (a) and (b), the function is overlaid with a scatter plot representing the mean and standard deviation of the dataset. (d) Explored points (i.e. the experimentally measured mechanical properties of each composite produced as indicated by the BO process) compared to literature, shown in a map of flexural strength σ_f versus stress intensity factors at crack initiation $K_{J,0}$ and limit $K_{J,lim}$. Black markers represent literature data on nacre-like ceramic composites [30,31,86], while colored markers show current data points, with colors indicating objective function values. A red circle highlights the material with the highest objective function, which reaches strength > 700 MPa and fracture toughness of > 13.6 MPa m$^{0.5}$. Light blue lines represent regions with constant objective function values, with arrows indicating growth direction. Error bars represent one standard deviation.

The pre-optimization analysis then confirms that the sol–gel – calcination – SPS processing strategy yields the desired nacre-like microstructures with alumina bricks well aligned and interfaced by a thin layer of tetragonal zirconia, which becomes more continuous as its vol% increases.

In the following sections, we explore findings from specimens made during the optimization phase, examining how the process parameters affected the final material. To streamline the naming convention for the tested compositions, we use a representation that indicates both the mortar content in wt.% and the ceria concentration in mol%. For instance, "10X_m-12x_{CeO_2}" denotes a composition with the 10 wt.% in mortar mass ratio and 12 mol% in CeO_2 mole percentage.

4.2. Material optimization

BO initialization. Our objective in material optimization was to determine the optimal values for ceria content x_{CeO_2}, mortar amount X_m, and dwell temperature T_{dwell} that maximize the objective function defined in Eq. (9). We selected reference parameters $\bar{K}_{J,lim}$ and $\bar{\sigma}_f$ with values of 16.9 MPa m$^{0.5}$ and 450 MPa, respectively. These values represented a well-balanced combination of mechanical properties for nacre-like alumina [49]. We set the weight parameter λ in Eq. (9) to 0.5 to achieve a balance between maximizing strength ($\lambda = 0$) and toughness ($\lambda = 1$). Additionally, we fixed the batch size at 3. Before initiating the optimization via BO, we selected an initial set of compositions to train the GP. We chose mortar mass fraction, X_m, ranging from 0 (alumina platelets only) to 30 wt.%, ceria mole fraction, x_{CeO_2}, up to 12 mol%, and dwell temperatures, T_{dwell}, below 1750 °C. The training points were then recursively expanded with each experiment, corresponding to an exploration point suggested by the acquisition strategy, with the goal of solving the optimization problem posed in Eq. (9).

Gaussian process and acquisition function. As an example of the procedure adopted, Fig. 3 illustrates the GP during the definition of the last batch of explored points. Fig. 3 (a, b) displays the GP posterior mean $\mu(\mathbf{x})$, and the GP posterior standard deviation $\sigma(\mathbf{x})$, alongside the mean and standard deviation of the training data set, respectively. The GP posterior mean revealed two local maxima at ceria concentrations of 4 and 10 mol% in orange–yellow regions (Fig. 3(a)). The GP posterior means calculated at these maxima exhibited different estimated

dispersions, as indicated by the respective standard deviations (Fig. 3(b)). Notably, the maximum at 4 mol% of ceria was situated in a relatively unexplored region, leading to a greater uncertainty in its estimated value. The acquisition function used $\mu(\mathbf{x})$ and $\sigma(\mathbf{x})$ to identify exploration points. Fig. 3(c) illustrates the values assumed by the acquisition function over three iterations for batch point exploration. In the left figure, the acquisition function is represented by the expected improvement per unit of cost EI_{pu}, which coincides with EI since the cost of the first exploration point is unitary. The function peaks at [13 wt.%, 4 mol%, 1600 °C], identifying the initial point of the batch $\mathbf{x}_1^b$. This selected point displayed a high a posteriori estimated value for the objective function and a substantial standard deviation, making it a favorable candidate for both exploration and exploitation strategies [37]. In the following figure, the selection of $\mathbf{x}_1^b$ was penalized by the penalty function φ_1. Consequently, the cost function is updated to prioritize the choice of an exploration point with the same composition, considering it more cost-effective. The maximization of the updated acquisition function leads to the selection of the next exploration point ($\mathbf{x}_2^b$ = [13 wt.%, 4 mol%, 1650 °C]), and this process is repeated for the third point ($\mathbf{x}_3^b$ = [13 wt.%, 4 mol%, 1550 °C]).

objective function and mechanical properties. The mechanical properties and corresponding values of the objective function for all sampled process parameter combinations are reported in Table S2 in the Supplementary Material, and summarized in Fig. 3(d). This figure shows the explored points - i.e. the experimentally measured mechanical properties of each composite produced with the process parameters suggested by the BO process. These are displayed in a diagram of flexural strength versus stress intensity factor at both crack initiation and limit, alongside analogous literature data for other types of nacre-like aluminas. The maximum point (obtained with 10 wt.% mortar with 6 mol% ceria and T_{dwell} = 1600 °C) achieves a mean value of flexural strength and stress intensity factor at the limit equal to 704 MPa and 13.6 MPa $m^{0.5}$, respectively. It exhibits superior strength compared not only to the tougher nacre-like aluminas, but also to pure Ce-TZP, which achieves an optimum fracture strength of approximately 500–600 MPa at 10–12 mol% CeO_2 [41], while maintaining very good fracture toughness. Spark plasma sintered alumina, on the other hand, can reach strength up to 450 MPa, but fracture toughness only up to 5.75 MPa $m^{0.5}$ [87]. We therefore successfully fabricated an all-ceramic nacre-like composite that outperforms both its constituents and other nacre-like aluminas in terms of combined strength and toughness.

While the optimization procedure could have continued to identify additional potential candidates as maximum points, we chose to interrupt the process due to the updated maximum EI, which was equal to 6%. It should be noted that within our Bayesian Optimization framework, the initial sampling conditions play a role in guiding the exploration of the parameter space. Although the method efficiently balances exploration and exploitation to identify optimal process parameters, it does not provide formal guarantees of global optimality. In principle, alternative initializations could lead to different local optima. However, performing multiple independent optimization and experimental campaigns would be impractical due to time and cost. Considering the excellent performance achieved relative to existing material benchmarks, we infer that the identified parameter set likely lies close to the global optimum, or at least represents a robust and practically meaningful local optimum for the targeted mechanical performance.

In the next two sections we analyze the process-structure-properties relations emerged by analyzing the experimental data relative to all double-tough ceramics produced and shown in Fig. 3(d).

4.3. Influence of process parameters on phase composition, microstructure and density

Phase composition and retention of tetragonal zirconia. The X-ray diffraction analysis of the sintered materials indicated the presence of α-Al_2O_3, t-ZrO_2, and m-ZrO_2 phases exclusively. By refining the spectra, we determined the quantities of each phase and their respective crystallite sizes. For a visual representation of the XRD spectra and the refinement outcomes, please see Figure S3 and Table S1 in the Supplementary Material. The alumina content exhibited a deviation from the nominal value, with a maximum difference of approximately 5%.

Fig. 4(a) illustrates the weight percentage of retained tetragonal zirconia in the mortar as a function of T_{dwell} for the various compositions. The remaining percentage consists of monoclinic zirconia formed from the tetragonal phase during sintering. The retained amount of tetragonal zirconia in the mortar exhibits a decreasing trend as T_{dwell} increases. This phenomenon is well-documented, as an increase in T_{dwell} promotes the growth of zirconia crystals, facilitating martensitic transformation [88,89].

This trend is influenced by both the amount of mortar and ceria content. In compositions featuring 10 wt.% mortar ($10X_m$-$6x_{CeO_2}$, $10X_m$-$8x_{CeO_2}$, $10X_m$-$10x_{CeO_2}$, and $10X_m$-$12x_{CeO_2}$), the retained tetragonal zirconia phase increases as ceria content rises for all T_{dwell} tested. Notably, there is a substantial reduction in the retained tetragonal zirconia amount with higher mortar contents. For mortar contents exceeding 13 wt.%, a sharp decline is observed, reaching levels of tetragonal zirconia in the mortar lower than 10 wt.% in the 30 wt.% mortar contents. The reduction in retained tetragonal zirconia with increasing mortar mass ratio can be attributed to autotransformation induced by tensile residual stress, as explained by Becher et al.'s theory [90]. According to their analytical model, zirconia particles embedded in an alumina matrix experience additional tensile residual stress transmitted through the matrix from neighboring zirconia particles. This reduces the external stress required to induce tetragonal to monoclinic transformation. The intensity of this additional residual stress is greater when zirconia particles are closer, as it decays with distance from each particle to the power of three. This phenomenon results in autotransformation of tetragonal zirconia particles when a critical amount of total transformable zirconia is reached.

In our study, sintering via spark plasma sintering allowed us to use a high heating rate and apply uniaxial pressure, improving densification and consequently reducing grain growth while enhancing the retention of tetragonal zirconia compared to conventional sintering [68,91–93]. This allowed us to surpass a 40 wt.% of retained tetragonal zirconia in the mortar at a T_{dwell} of 1750 °C. The use of high-pressure spark plasma sintering could further increase the quantity of retained tetragonal zirconia [94,95]. An analysis of the crystallite size of both tetragonal and monoclinic phases confirms the identified trends (see Supplementary Materials, Section 5 and Fugure S3).

Density. Fig. 4(b) illustrates the final relative density (ρ_r) values as a function of T_{dwell}. The trend of ρ_r with varying T_{dwell} shows distinct variations among the tested compositions. Overall, ρ_r increases with T_{dwell} up to an optimum value, beyond which a slight decrease is observed for some compositions. The reduction in ρ_r at high T_{dwell} may be attributed to the tetragonal to monoclinic transformation in the zirconia phase which, leading to a growth of the grain and the formation of microcracks, results in a decrease in the final relative density [96]. Notably, the onset of decreasing in ρ_r occurred at a lower T_{dwell} for the specimen with composition $10X_m$-$6x_{CeO_2}$ compared to the $10X_m$-$8x_{CeO_2}$. The lower content of stabilizing ceria here leads to a rapid transformation into monoclinic with increasing T_{dwell}.

The addition of mortar significantly influences ρ_r, with a general trend of increased mortar amounts promoting densification. Notably, specimens with composition $0X_m$-$0x_{CeO_2}$ exhibit lower ρ_r values than those with a non-zero mortar percentage for T_{dwell} less than 1750°C. A comparison of the effect of mortar addition on ρ_r at the same ceria concentration can be made among the specimens with compositions $5X_m$-$6x_{CeO_2}$, $10X_m$-$6x_{CeO_2}$, and $20X_m$-$6x_{CeO_2}$. The specimen with composition $10X_m$-$6x_{CeO_2}$ achieves the highest ρ_r value compared to those with 5 wt.% and 20 wt.% of mortar. At lower mortar contents (5 wt.%)

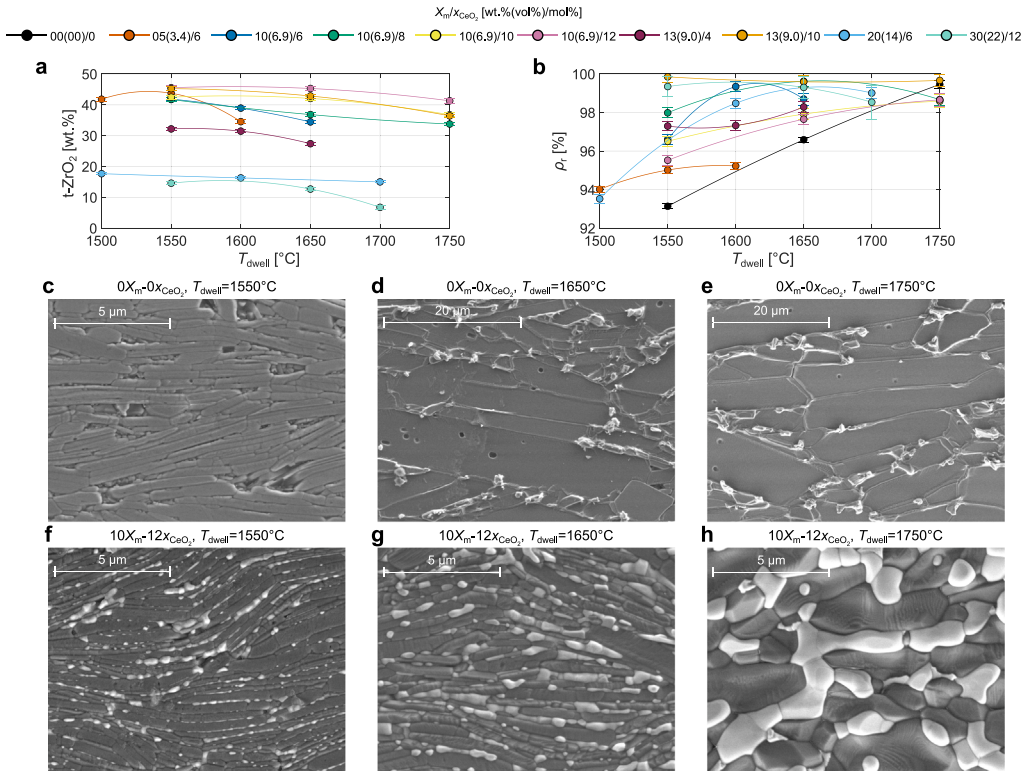

Fig. 4. Process parameters effects on phase composition, density and microstructure. (a) percentage by weight of the t-ZrO_2 phase in the mortar, and (b) variation of the final relative density (ρ_r) as a function of dwell temperature (T_{dwell}) for different tested combinations of mortar mass ratio (X_m), with the volume ratio also indicated in brackets, and ceria mole fraction (x_{CeO_2}). Error bars represent one standard deviation. SEM micrographs (c–e) and (f–h) reveal the microstructures of samples with compositions $0X_m$–$0x_{CeO_2}$ and $10X_m$–$12x_{CeO_2}$, respectively, sintered at dwell temperatures of 1550 °C (e, h), 1650 °C (f, i), and 1750 °C (g, j). The images highlight how the introduction of mortar constrains the growth of alumina platelets. As T_{dwell} increases, the microstructure gradually loses its distinctive "brick-and-mortar" pattern. Thermal etching was performed at a temperature 150 °C below the corresponding T_{dwell}. SEM images were captured under low vacuum conditions with a chamber pressure of 0.6 bar, a working distance of 5 mm, a beam voltage of 5 kV, and a spot size of 2.5.

the mortar is not uniform, while at higher contents (20 wt.%) it ends up containing a more considerable amount of monoclinic zirconia.

A comparison, instead, of the effect of ceria addition on ρ_r with the same mortar amount can be made among the specimens with compositions $10X_m$-$6x_{CeO_2}$, $10X_m$-$8x_{CeO_2}$, $10X_m$-$10x_{CeO_2}$, and $10X_m$-$12x_{CeO_2}$. As ceria concentration increases up to 8 mol%, an increase in the maximum ρ_r is observed. A further increase in ceria concentration results in a decrease in the maximum ρ_r. In the literature, there are different explanations for the effects of ceria addition on the final relative density. The increase in ρ_r with increasing ceria content [57,97], is attributed to the higher mass density of ceria and an increase in the retained tetragonal zirconia phase within the final microstructure, which is denser than the monoclinic counterpart. The potential decline in ρ_r at higher ceria concentrations was associated with the formation of elongated grains of $CeAl_{11}O_{18}$ [97], a decrease in grain boundary diffusion [98], or the formation of agglomerates [99]. In the current study, the formation of elongated grains of $CeAl_{11}O_{18}$ is to be excluded, since XRD spectra and micrograph analyses revealed no evidence of elongated grains from other phases, therefore pointing towards reduced grain boundary diffusion or the presence of localized agglomerates.

Microstructure and grain growth. Fig. 4(c–h) presents SEM micrographs illustrating the microstructures of samples with compositions $0X_m$-$0x_{CeO_2}$ (upper figures) and $10X_m$-$12x_{CeO_2}$ (lower figures), where the lighter phase is the zirconia mortar. The samples were sintered at T_{dwell} temperatures of 1550, 1650, and 1750 °C. A comparison of Fig. 4(c–e), where different scale bars are used, reveals a significant increase in grain size with the growth of T_{dwell}. In Fig. 4(f–h), the samples were sintered at the same T_{dwell} temperatures as those above, emphasizing the mortar's role as a pinning phase that restricts the growth of alumina platelets [100]. However, as T_{dwell} increases, the microstructure undergoes a transformation, losing its distinctive "brick and mortar" characteristic. At the highest T_{dwell}, it exhibits agglomerates of zirconia grains dispersed in an alumina matrix.

4.4. Influence of process parameters on mechanical properties

R-curve behavior and synergy of multiple toughening mechanisms. The double-tough ceramics, as desired, feature R-curve behavior. Fig. 5(a–c) shows the R-curves, and the corresponding crack path of specimens without (a) and with mortar (10 wt.%) (b, c) for two different ceria contents. In the first case (Fig. 5(a)), the crack was repeatedly deflected until it traversed the entire sample. In contrast, in Fig. 5(c), the crack was initially deflected but later aligned with the loading direction, showing smaller deviations. A similar trend was observed in Fig. 5(b), where stable propagation was limited. The corresponding fractographies in Fig. 5 (d–f) reveal mixed crack patterns, with samples containing a nonzero mortar fraction exhibiting predominantly transgranular (TG) features accompanied by localized failure at the alumina–zirconia interfaces. Therefore, crack deflection dominated the initial phase of propagation in samples containing mortar, while stable crack propagation throughout the mechanical test was attributed to transformation toughening mechanisms. No clear correlation between toughness and deflection angle was observed, and the crack deflection in our material is moderate compared to other studies [49], where the deflection is more pronounced and represents the dominant toughening mechanism. This behavior aligns well with the findings of Dimas et al. who used a mesoscale bead model of a brick-and-mortar composite with linear elastic constituents to investigate its deformation and failure

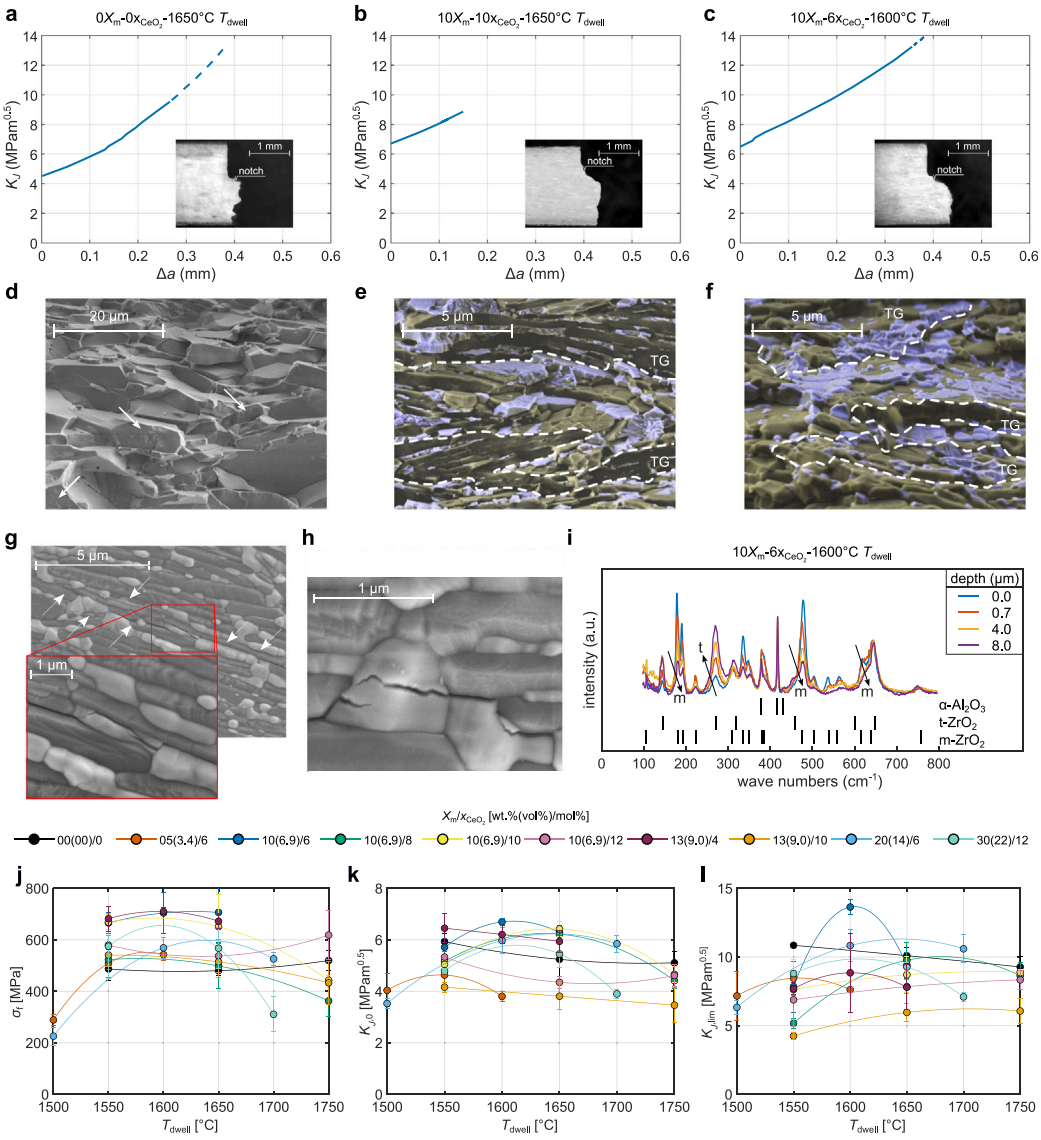

Fig. 5. Process parameter effects on mechanical properties and fracture behavior. R-curves for specimens with (a) and without mortar (b, c) for varying ceria content, with SEM fractographs (d, e, f). Dashed lines in the R-curves show data exceeding the crack extension limit of $0.25(W - a_0)$ [83]. Arrows in (d) indicate platelet fracture, while "TG" in (e, f) marks transgranular fracture. (g) and (h) show a secondary crack passing through the mortar phase in a sample sintered at 1700 °C. In (g), arrows indicate the crack path, while (h) highlights a zirconia particle acting as a crack bridge (material with composition $20X_m$-$6x_{CeO_2}$). SEM images were taken under low vacuum (0.6 bar, 5 kV, 5 mm working distance). (i) shows Raman analysis performed on the fracture surface of the specimen with the optimal composition ($10X_m$-$6x_{CeO_2}$, sintered at a T_{dwell} of 1600°C). The arrows indicate that the fraction of untransformed tetragonal zirconia increases with distance (depth) from the fracture surface (peak indexing performed in accordance with [101,102]). Variations in flexural strength (σ_f) (j), stress intensity at crack initiation ($K_{J,0}$) (k), and limit ($K_{J,lim}$) (l) are shown for different mortar ratios (X_m) and ceria content (x_{CeO_2}). Error bars indicate one standard deviation.

mechanisms. In our material, the stiffness ratio between the mortar phase and the alumina bricks is approximately 0.45, leading to a crack path that alternates between the brick and mortar phases rather than following a highly tortuous trajectory [103].

Additional toughening mechanisms are visible in Fig. 5 (g, h) (material with composition $20X_m$-$6x_{CeO_2}$), which shows secondary cracks branching from the main one. Arrows in Fig. 5(g) trace the crack path across the brick–mortar interfaces, highlighting intersections with the mortar phase, while Fig. 5(h) shows zirconia particles bridging the crack faces, dissipating energy and enhancing the material's toughness.

To confirm the presence of stress-induced tetragonal-to-monoclinic phase transformation, we performed Raman spectroscopy on the fracture surface of the material with composition $10X_m$-$6x_{CeO_2}$, sintered at 1600 °C, which achieved the highest value of the objective function. Fig. 5(i) presents the Raman spectra measured at various depths. We started from the surface of the fracture (depth 0) and subsequently probed at increasing depths underneath the same area. The intensity of the peaks corresponding to the tetragonal zirconia phase increases with depth, while the intensity of the monoclinic zirconia peaks decreases. This behavior is consistent with the phenomenon of stress-induced tetragonal-to-monoclinic phase transformation. The stress field generated during stable crack propagation intensifies near the crack, causing the tetragonal-to-monoclinic transformation in the material surrounding the crack [104]. Consequently, the amount of transformed monoclinic phase decreases as the analysis moves deeper into the material where the experienced stresses have been lower. This

trend was verified in two separate areas of the fracture surface of the same material (see Supplementary Material Figure S5).

Flexural strength and fracture toughness. The stress intensity factors for both crack initiation ($K_{J,0}$) and limit ($K_{J,\mathrm{lim}}$), along with the flexural strength (σ_f), obtained from three-point bending tests on smooth specimens are summarized in Table S2 in the Supplementary Material. Notably, the three repetitions of mechanical tests showed very limited dispersion of results. Fig. 5(j) shows the variation of σ_f as a function of T_{dwell} for the tested compositions. The σ_f values of the sample with composition $0X_m$-$0x_{CeO_2}$ remain approximately constant as the T_{dwell} varies. Although the final relative density of the composition $0X_m$-$0x_{CeO_2}$ shows a significant increase as the T_{dwell} increases (Fig. 4(d)), the reduction of pore defects associated with the increase in final relative density does not lead to an improvement in mechanical properties due to the increase in platelet size (Fig. 4 (e–j)). In general, the addition of mortar increased σ_f in the T_{dwell} range between 1550 and 1650 °C. At higher dwell temperatures, grain growth and microcracking due to the tetragonal to monoclinic phase transformation lead to a strength reduction. The highest σ_f values are measured for sample $13X_m$-$4x_{CeO_2}$, which has the lowest ceria content, sintered at 1600 °C. Stress intensity factors at both crack initiation and limit, as functions of T_{dwell}, are shown in Fig. 5(k), and (l). The tested compositions generally exhibit an initial increase in both $K_{J,0}$ and $K_{J,\mathrm{lim}}$ as T_{dwell} increases, followed by reaching a maximum and subsequently decreasing with further increases in T_{dwell}. The initial rise in $K_{J,0}$ and $K_{J,\mathrm{lim}}$ with increasing T_{dwell} is expected due to the reduction in material porosity. With a further increase in T_{dwell}, excessive grain growth triggers a tetragonal to monoclinic phase transformation in the zirconia phase during sintering. This transformation induces microcracks and reduces transformation toughening due to a lower amount of tetragonal zirconia in the final composition. These phenomena correlate to the previous observations on phase composition, density and microstructure (Fig. 4 (c, d)). Specimens without mortar ($0X_m$-$0x_{CeO_2}$) and those with a very stable tetragonal phase ($10X_m$-$10x_{CeO_2}$, $10X_m$-$12x_{CeO_2}$, and $13X_m$-$10x_{CeO_2}$) exhibited little to no reduction in $K_{J,0}$ and $K_{J,\mathrm{lim}}$, consistent with the absence or limited extent of the tetragonal-to-monoclinic phase transformation during crack propagation.

At a temperature of 1600 °C, the specimen with composition $10X_m$-$6x_{CeO_2}$, demonstrates the highest $K_{J,\mathrm{lim}}$ value, 13.6 MPa m$^{0.5}$, which is remarkably high for ceramics. It corresponds to a 400% increase with respect to the micro-scale fracture toughness of alumina grains in textured alumina ceramics [105]. Although, as shown in Fig. 3(d), there are nacre-like composites with higher toughness (16.9 MPa m$^{0.5}$), these possess significantly lower strength. As shown by the Raman analysis performed on the fracture surface (Fig. 5(i)), the stress-induced tetragonal-to-monoclinic phase transformation is present in the material. Therefore, we can attribute a contribution to the toughness to this stress-induced transformation. The specimen with composition $10X_m$-$6x_{CeO_2}$ shows large crystal sizes at 1600, °C (Fig. 4(a)) and a rapid spontaneous transformation of the tetragonal phase with increasing T_{dwell} (Fig. 4(c)), suggesting that the crystal size approached the critical threshold for spontaneous tetragonal-to-monoclinic transformation, thereby enhancing the mechanical properties [106]. It is also worth noting that monoclinic zirconia can contribute to the increase in toughness in zirconia-toughened alumina through the nucleation of microcracks that occur in the stress field of propagating cracks [107].

5. Conclusions

We engineered an ultra-strong "double-tough" ceramic consisting of nacre-like alumina with ceria-stabilized zirconia as a mortar phase. Utilizing a sol–gel technique followed by calcination, we successfully produced nanograined tetragonal zirconia uniformly distributed around the platelets. After spark plasma sintering, we achieved bulk materials with platelets oriented in a brick and mortar microstructure. To expedite the experimental campaign aimed at finding the optimal process parameters (ceria concentration, mortar amount, and dwell temperature), we developed a batch Bayesian Optimization framework that maximized the balance between strength and toughness. Exploring ten compositions and thirty different sets of processing parameters allowed us to increase the objective function value by 38% compared to the all-alumina material and by 31% compared to the initial set.

Leveraging transformation toughening at the nanoscale and crack deflection at the microscale, the materials achieved exceptional fracture toughness (> 13.5 MPa m$^{0.5}$) and strength (> 700 MPa) along with a stress intensity factor at crack initiation of 6.7 MPa m$^{0.5}$. Notably, the only reported nacre-like alumina surpassing this fracture toughness values has strength levels well below 500 MPa. The achieved combination of strength and toughness also outperforms zirconia, delivering higher strength at comparable fracture toughness. This was achieved with process parameters identified using Bayesian optimization. Further optimization is possible by adjusting strength and toughness weights in the BO objective function.

Additional insights are:

- The zirconia mortar contributes to densify the material, especially at lower dwell temperatures, where transformation is minimized, and it additionally acts as a pinning phase for alumina grain growth and increasing flexural strength.
- Increasing dwell temperature improves density up to a point; beyond this, relative density decreases, and the "brick-and-mortar" structure is lost. The percentage of retained tetragonal zirconia follows the same trend. These effects are reflected in the measured strength and fracture toughness, which tend to peak at the intermediate SPS dwell temperatures.
- Spark plasma sintering allows the retention of over 40 wt.% of retained tetragonal zirconia at 1750 °C. High-pressure spark plasma sintering can further enhance tetragonal phase retention.
- Ceria stabilizes the tetragonal phase of zirconia. However, at high ceria contents, the hindered transformation to monoclinic zirconia limits toughness by reducing the contribution from transformation toughening.

The proposed process optimization framework not only expedites the material design but also serves as a promising pathway for the development of materials with tailored and improved mechanical properties. Exploring additional process parameters, such as alumina platelet size and alternative stabilizers, could further optimize performance. The applicability of the proposed methodology also extends well beyond the concept of double-tough ceramics, serving as valuable optimization framework for a variety of cumbersome, time and energy-intensive experimental processes.

CRediT authorship contribution statement

Francesco Aiello: Writing – review & editing, Writing – original draft, Visualization, Validation, Methodology, Investigation, Formal analysis, Data curation. **Jian Zhang:** Writing – review & editing, Investigation. **Johannes C. Brouwer:** Writing – review & editing, Investigation. **Michele Cassetta:** Writing – review & editing, Investigation. **Mauro Salazar:** Writing – review & editing, Supervision, Project administration, Methodology, Investigation, Funding acquisition, Conceptualization. **Diletta Giuntini:** Writing – review & editing, Supervision, Resources, Project administration, Methodology, Investigation, Funding acquisition, Conceptualization.

Declaration of competing interest

The authors declare that they have no known competing financial interests or personal relationships that could have appeared to influence the work reported in this paper.

Acknowledgments

We gratefully acknowledge the financial support from the Dutch Sectorplan, Zwaartepunt Mechanics of Materials and Zwaartepunt Control Systems Technology. DG gratefully acknowledges the financial support from the Institute of Complex Molecular Systems of TU/e and the Irene Curie Fellowship. The authors would like to thank the "Centro Piattaforme Tecnologiche" of the University of Verona (Italy) for technical support, and Prof. Francesco Maresca and Prof. Marc Geers for their valuable input on the article writing.

Appendix A. Supplementary data

Supplementary material related to this article can be found online at https://doi.org/10.1016/j.actamat.2025.121878.

Data availability

Data are available in the Supplementary Material or can be obtained from the authors upon request.

References

[1] J. Rösler, H. Harders, M. Bäker, Mechanical Behaviour of Engineering Materials: Metals, Ceramics, Polymers, and Composites, Springer Berlin, Heidelberg, 2007.
[2] R.O. Ritchie, The conflicts between strength and toughness, Nat. Mater. 10 (11) (2011) 817–822.
[3] W. Huang, D. Restrepo, J.-Y. Jung, F.Y. Su, Z. Liu, R.O. Ritchie, J. McKittrick, P. Zavattieri, D. Kisailus, Multiscale toughening mechanisms in biological materials and bioinspired designs, Adv. Mater. 31 (43) (2019) 1901561.
[4] D.J. Green, Transformation Toughening of Ceramics, CRC Press, Boca Raton, 2018.
[5] A. Plunkett, K. Temiz, C. Warren, V. Wisniewski, K.P. Furlan, J. Garay, D. Giuntini, B. Domènech, G.A. Schneider, Bridging nanocrystals to robust, multifunctional, bulk materials through nature-inspired, hierarchical design, 2022, ChemRxiv.
[6] B. Bor, L. Heilmann, B. Domènech, M. Kampferbeck, T. Vossmeyer, H. Weller, G.A. Schneider, D. Giuntini, Mapping the mechanical properties of hierarchical supercrystalline ceramic-organic nanocomposites, Molecules 25 (20) (2020) 4790.
[7] T. Magrini, F. Bouville, A. Lauria, H. Le Ferrand, T.P. Niebel, A.R. Studart, Transparent and tough bulk composites inspired by nacre, Nat. Commun. 10 (1) (2019) 2794.
[8] T. Magrini, S. Moser, M. Fellner, A. Lauria, F. Bouville, A.R. Studart, Transparent nacre-like composites toughened through mineral bridges, Adv. Funct. Mater. 30 (27) (2020) 2002149.
[9] M. Grossman, F. Bouville, F. Erni, K. Masania, R. Libanori, A.R. Studart, Mineral nano-interconnectivity stiffens and toughens nacre-like composite materials, Adv. Mater. 29 (8) (2017) 1605039.
[10] E. Poloni, F. Bouville, C.H. Dreimol, T.P. Niebel, T. Weber, A.R. Biedermann, A.M. Hirt, A.R. Studart, Tough metal–ceramic composites with multifunctional nacre-like architecture, Sci. Rep. 11 (1) (2021) 1621.
[11] T. Magrini, A. Senol, R. Style, F. Bouville, A.R. Studart, Fracture of hierarchical multi-layered bioinspired composites, J. Mech. Phys. Solids 159 (2022) 104750.
[12] X.Y. Chan, C. Chua, S. Tan, H. Le Ferrand, Energy dissipation in composites with hybrid nacre-like helicoidal microstructures, Compos. Part B: Eng. 232 (2022) 109608.
[13] H. Zhao, L. Guo, Nacre-inspired structural composites: performance-enhancement strategy and perspective, Adv. Mater. 29 (45) (2017) 1702903.
[14] X. Luo, K. Zhao, X. He, Y. Bai, V. De Andrade, M. Zaiser, L. An, J. Liu, Evading strength and ductility trade-off in an inverse nacre structured magnesium matrix nanocomposite, Acta Mater. 228 (2022) 117730.
[15] J. Sun, B. Bhushan, Hierarchical structure and mechanical properties of nacre: a review, Rsc Adv. 2 (20) (2012) 7617–7632.
[16] M. Grossman, F. Bouville, K. Masania, A.R. Studart, Quantifying the role of mineral bridges on the fracture resistance of nacre-like composites, Proc. Natl. Acad. Sci. 115 (50) (2018) 12698–12703.
[17] M. Grossman, D. Pivovarov, F. Bouville, C. Dransfeld, K. Masania, A.R. Studart, Hierarchical toughening of nacre-like composites, Adv. Funct. Mater. 29 (9) (2019) 1806800.
[18] R. Wang, Z. Suo, A. Evans, N. Yao, I.A. Aksay, Deformation mechanisms in nacre, J. Mater. Res. 16 (9) (2001) 2485–2493.
[19] K. Radi, H. Saad, D. Jauffrès, S. Meille, T. Douillard, S. Deville, C.L. Martin, Effect of microstructure heterogeneity on the damage resistance of nacre-like alumina: insights from image-based discrete simulations, Scr. Mater. 191 (2021) 210–214.
[20] H. Saad, T. Douillard, A. Malchère, P. Steyer, S. Meille, S. Deville, B. Reynard, Toughening mechanisms in nacre-like alumina revealed by in-situ imaging of stress, J. Eur. Ceram. Soc. 42 (14) (2022) 6757–6761.
[21] E. Feilden, T. Giovannini, N. Ni, C. Ferraro, E. Saiz, L. Vandeperre, F. Giuliani, Micromechanical strength of individual Al2O3 platelets, Scr. Mater. 131 (2017) 55–58.
[22] S. Deville, A.P. Tomsia, S. Meille, Complex composites built through freezing, Acc. Chem. Res. 55 (11) (2022) 1492–1502.
[23] R.P. Wilkerson, B. Gludovatz, J. Watts, A.P. Tomsia, G.E. Hilmas, R.O. Ritchie, A study of size effects in bioinspired, nacre-like, metal-compliant-phase (nickel-alumina) coextruded ceramics, Acta Mater. 148 (2018) 147–155.
[24] I. Corni, T. Harvey, J. Wharton, K. Stokes, F. Walsh, R. Wood, A review of experimental techniques to produce a nacre-like structure, Bioinspiration Biomimetics 7 (3) (2012) 031001.
[25] H. Le Ferrand, B.T. Goh, S.-H. Teoh, Nacre-like ceramic composites: properties, functions and fabrication in the context of dental restorations, Acta Biomater. (2023).
[26] H. Le Ferrand, F. Bouville, Processing of dense bioinspired ceramics with deliberate microstructure, J. Am. Ceram. Soc. 102 (12) (2019) 7253–7263.
[27] K. Evers, S. Falco, N. Grobert, R.I. Todd, Nacre-like alumina with unique high strain rate capabilities, J. Eur. Ceram. Soc. 40 (2) (2020) 417–426.
[28] W. Clegg, K. Kendall, N.M. Alford, T. Button, J. Birchall, A simple way to make tough ceramics, Nature 347 (6292) (1990) 455–457.
[29] T.P. Niebel, F. Bouville, D. Kokkinis, A.R. Studart, Role of the polymer phase in the mechanics of nacre-like composites, J. Mech. Phys. Solids 96 (2016) 133–146.
[30] F. Bouville, E. Maire, S. Meille, B. Van de Moortèle, A.J. Stevenson, S. Deville, Strong, tough and stiff bioinspired ceramics from brittle constituents, Nat. Mater. 13 (5) (2014) 508–514.
[31] P.I. Pelissari, F. Bouville, V.C. Pandolfelli, D. Carnelli, F. Giuliani, A.P. Luz, E. Saiz, A.R. Studart, Nacre-like ceramic refractories for high temperature applications, J. Eur. Ceram. Soc. 38 (4) (2018) 2186–2193.
[32] P. Pelissari, V.C. Pandolfelli, D. Carnelli, F. Bouville, Refractory interphase and its role on the mechanical properties of boron containing nacre-like ceramic, J. Eur. Ceram. Soc. 40 (1) (2020) 165–172.
[33] W. Pabst, G. Ticha, E. Gregorová, Effective elastic properties of alumina-zirconia composite ceramics-part 3. calculation of elastic moduli of polycrystalline alumina and zirconia from monocrystal data, Ceramics- Silik. 48 (2) (2004) 41–48.
[34] R. Henry, H. Saad, S. Dankic-Cottrino, S. Deville, S. Meille, Nacre-like alumina composites reinforced by zirconia particles, J. Eur. Ceram. Soc. 42 (5) (2022) 2319–2330.
[35] V. Vilchez, P.I. Pelissari, V.C. Pandolfelli, F. Bouville, Mixed-mode fracture model to quantify local toughness in nacre-like alumina, J. Eur. Ceram. Soc. 43 (10) (2023) 4472–4481.
[36] R.C. Garvie, Thermodynamic analysis of the tetragonal to monoclinic transformation in a constrained zirconia microcrystal: Part 2 in the presence of an applied stress, J. Mater. Sci. 20 (1985) 3479–3486.
[37] R. Garnett, Bayesian Optimization, Cambridge University Press, Cambridge, 2023.
[38] M. Diessner, J. O'Connor, A. Wynn, S. Laizet, Y. Guan, K. Wilson, R.D. Whalley, Investigating bayesian optimization for expensive-to-evaluate black box functions: Application in fluid dynamics, Front. Appl. Math. Stat. 8 (2022) 1076296.
[39] K. Park, C. Song, J. Park, S. Ryu, Multi-objective bayesian optimization for the design of nacre-inspired composites: optimizing and understanding biomimetics through ai, Mater. Horizons (2023).
[40] J. Zhang, F. Aiello, M. Salazar, D. Giuntini, Double-tough ceramics: Optimization-supported multiscale computational design, Acta Mater. 296 (2025) 121162.
[41] J. Chevalier, A. Liens, H. Reveron, F. Zhang, P. Reynaud, T. Douillard, L. Preiss, V. Sergo, V. Lughi, M. Swain, et al., Forty years after the promise of «ceramic steel?»: Zirconia-based composites with a metal-like mechanical behavior, J. Am. Ceram. Soc. 103 (3) (2020) 1482–1513.
[42] J. Chevalier, L. Gremillard, Ceramics for medical applications: A picture for the next 20 years, J. Eur. Ceram. Soc. 29 (7) (2009) 1245–1255.
[43] I. Touaiher, M. Saâdaoui, J. Chevalier, L. Preiss, H. Reveron, Fracture behavior of ce-tzp/alumina/aluminate composites with different amounts of transformation toughening. influence of the testing methods, J. Eur. Ceram. Soc. 38 (4) (2018) 1778–1789.
[44] P. Kohorst, L. Borchers, J. Strempel, M. Stiesch, T. Hassel, F.-W. Bach, C. Hübsch, Low-temperature degradation of different zirconia ceramics for dental applications, Acta Biomater. 8 (3) (2012) 1213–1220.
[45] B. Inserra, B. Coppola, L. Montanaro, J.-M. Tulliani, P. Palmero, Preparation and characterization of Ce-ZrO2/Al2O3 composites by dlp-based stereolithography, J. Eur. Ceram. Soc. 43 (7) (2023) 2907–2916.

[46] P. Budarapu, S. Thakur, S. Kumar, M. Paggi, Micromechanics of engineered interphases in nacre-like composite structures, Mech. Adv. Mater. Struct. 28 (22) (2021) 2327–2342.
[47] R.C. Garvie, M.V. Swain, Thermodynamics of the tetragonal to monoclinic phase transformation in constrained zirconia microcrystals: Part 1 in the absence of an applied stress field, J. Mater. Sci. 20 (1985) 1193–1200.
[48] R. Castro, K. Van Benthem, Sintering: Mechanisms of Convention Nanodensification and Field Assisted Processes, vol. 35, Springer Berlin, Heidelberg, 2012.
[49] F. Bouville, Strong and tough nacre-like aluminas: Process–structure–performance relationships and position within the nacre-inspired composite landscape, J. Mater. Res. 35 (8) (2020) 1076–1094.
[50] F. Sommer, R. Landfried, F. Kern, R. Gadow, Mechanical properties of zirconia toughened alumina with 10–24 % 1.5 mol% Y-TZP reinforcement, J. Eur. Ceram. Soc. 32 (15) (2012) 3905–3910.
[51] A. De Aza, J. Chevalier, G. Fantozzi, M. Schehl, R. Torrecillas, Crack growth resistance of alumina, zirconia and zirconia toughened alumina ceramics for joint prostheses, Biomaterials 23 (3) (2002) 937–945.
[52] O.Y. Zadorozhnaya, T. Khabas, O. Tiunova, S. Malykhin, Effect of grain size and amount of zirconia on the physical and mechanical properties and the wear resistance of zirconia-toughened alumina, Ceram. Int. 46 (7) (2020) 9263–9270.
[53] S. Pfeifer, P. Demirci, R. Duran, H. Stolpmann, A. Renfftlen, S. Nemrava, R. Niewa, B. Clauß, M.R. Buchmeiser, Synthesis of zirconia toughened alumina (ZTA) fibers for high performance materials, J. Eur. Ceram. Soc. 36 (3) (2016) 725–731.
[54] F. Lange, Transformation toughening: Part 4 fabrication, fracture toughness and strength of Al 2 O 3-ZrO 2 composites, J. Mater. Sci. 17 (1982) 247–254.
[55] I. Nettleship, R. Stevens, Tetragonal zirconia polycrystal (TZP)—A review, Int. J. High Technol. Ceram. 3 (1) (1987) 1–32.
[56] E. Tani, M. Yoshimura, s. Somiya, Revised phase diagram of the system ZrO2-CeO2 below 1400° c, J. Am. Ceram. Soc. 66 (7) (1983) 506–510.
[57] A.L. Quinelato, E. Longo, L.A. Perazolli, J.A. Varela, Effect of ceria content on the sintering of ZrO2 based ceramics synthesized from a polymeric precursor, J. Eur. Ceram. Soc. 20 (8) (2000) 1077–1084.
[58] M. Rezaei, S. Alavi, S. Sahebdelfar, Z.-F. Yan, Synthesis of ceria doped nanozirconia powder by a polymerized complex method, J. Porous Mater. 16 (2009) 497–505.
[59] G. Grathwohl, T. Liu, Crack resistance and fatigue of transforming ceramics: Ii, CeO2-stabilized tetragonal ZrO2, J. Am. Ceram. Soc. 74 (12) (1991) 3028–3034.
[60] T. Liu, Y.W. Mai, M. Swain, G. Grathwohl, Effects of grain size and specimen geometry on the transformation and R-curve behaviour of 9Ce-TZP ceramics, J. Mater. Sci. 29 (1994) 835–843.
[61] A. Liens, H. Reveron, T. Douillard, N. Blanchard, V. Lughi, V. Sergo, R. Laquai, B.R. Müller, G. Bruno, S. Schomer, et al., Phase transformation induces plasticity with negligible damage in ceria-stabilized zirconia-based ceramics, Acta Mater. 183 (2020) 261–273.
[62] M. Fornabaio, R. Traverso, P. Palmero, H. Reveron, J. Chevalier, L. Montanaro, Zirconia-based composites with tailored composition and architecture: elaboration and microstructural characterization, in: 14th European Inter-Regional Conference on Ceramics, CIEC14, 2014.
[63] S. Sharma, N. Gokhale, R. Dayal, R. Lal, Synthesis, microstructure and mechanical properties of ceria stabilized tetragonal zirconia prepared by spray drying technique, Bull. Mater. Sci. 25 (2002) 15–20.
[64] M. Orlovska, L. Húlek, L. Bača, V. Kovar, K. Tomanova, M. Kitzmantel, M. Janek, E. Neubauer, Study of the alumina sintering process with a low zirconia content, Ceram. Int. 48 (2) (2022) 2736–2743.
[65] J. González, Z. Dai, P. Hennig, N. Lawrence, Batch bayesian optimization via local penalization, in: Artificial Intelligence and Statistics, PMLR, 2016, pp. 648–657.
[66] R. Shen, S.N. Shafrir, C. Miao, M. Wang, J.C. Lambropoulos, S.D. Jacobs, H. Yang, Synthesis and corrosion study of zirconia-coated carbonyl iron particles, J. Colloid Interface Sci. 342 (1) (2010) 49–56.
[67] S. Rossignol, Y. Madier, D. Duprez, Preparation of zirconia–ceria materials by soft chemistry, Catal. Today 50 (2) (1999) 261–270.
[68] O. Guillon, J. Gonzalez-Julian, B. Dargatz, T. Kessel, G. Schierning, J. Räthel, M. Herrmann, Field-assisted sintering technology/spark plasma sintering: mechanisms, materials, and technology developments, Adv. Eng. Mater. 16 (7) (2014) 830–849.
[69] D. Giuntini, E.A. Olevsky, C. Garcia-Cardona, A.L. Maximenko, M.S. Yurlova, C.D. Haines, D.G. Martin, D. Kapoor, Localized overheating phenomena and optimization of spark-plasma sintering tooling design, Materials 6 (7) (2013) 2612–2632.
[70] A.B. Spierings, M. Schneider, R. Eggenberger, Comparison of density measurement techniques for additive manufactured metallic parts, Rapid Prototyp. J. 17 (5) (2011) 380–386.
[71] N.S.R.D..N.C. WebBook, Thermophysical properties of fluid systems, isobaric properties for water, 2008, https://webbook.nist.gov/chemistry/fluid/.
[72] Y. Liu, P.H. Daum, Relationship of refractive index to mass density and self-consistency of mixing rules for multicomponent mixtures like ambient aerosols, J. Aerosol Sci. 39 (11) (2008) 974–986.
[73] D.L. Perry, Handbook of Inorganic Compounds, CRC Press, Boca Raton, 2016.
[74] C. Murti, U. Maslakah, E. Endarko, T. Triwikantoro, Structural, physical and mechanical properties of zirconia-polymorph/alumina composites, Mater. Chem. Phys. 285 (2022) 126102.
[75] P. Mallick, Fiber-reinforced composites: Materials, manufacturing, and design, 2007.
[76] R.E. Chinn, Preparation and analysis of ceramic microstructures, Mater. Park: ASM Int. (2002).
[77] B.H. Toby, R.B. Von Dreele, Gsas-ii: the genesis of a modern open-source all purpose crystallography software package, J. Appl. Crystallogr. 46 (2) (2013) 544–549.
[78] N. Igawa, Y. Ishii, Crystal structure of metastable tetragonal zirconia up to 1473 K, J. Am. Ceram. Soc. 84 (5) (2001) 1169–1171.
[79] H. Fukui, M. Fujimoto, Y. Akahama, A. Sano-Furukawa, T. Hattori, Structure change of monoclinic ZrO2 baddeleyite involving softenings of bulk modulus and atom vibrations, Acta Crystallogr. Sect. B: Struct. Sci. Cryst. Eng. Mater. 75 (4) (2019) 742–749.
[80] E.N. Maslen, V. Streltsov, N. Streltsova, N. Ishizawa, Y. Satow, Synchrotron X-ray study of the electron density in α-Al2O3, Acta Crystallogr. Sect. B: Struct. Sci. 49 (6) (1993) 973–980.
[81] S. Gražulis, D. Chateigner, R.T. Downs, A.F.T. Yokochi, M. Quirós, L. Lutterotti, E. Manakova, J. Butkus, P. Moeck, A. Le Bail, Crystallography open database – an open-access collection of crystal structures, J. Appl. Crystallogr. 42 (4) (2009) 726–729, http://dx.doi.org/10.1107/S0021889809016690.
[82] ISO 14704:2016: Fine Ceramics (Advanced Ceramics, Advanced Technical Ceramics) - Test Method for Flexural Strength of Monolithic Ceramics at Room Temperature, Standard, International Organization for Standardization, Geneva, CH, 2016.
[83] ISO 12135:2021: Metallic Materials - Unified Method of Test for the Determination of Quasistatic Fracture Toughness, Standard, International Organization for Standardization, Geneva, CH, 2021.
[84] H. Narayanan, F. Dingfelder, I. Condado Morales, B. Patel, K.E. Heding, J.R. Bjelke, T. Egebjerg, A. Butté, M. Sokolov, N. Lorenzen, et al., Design of biopharmaceutical formulations accelerated by machine learning, Mol. Pharm. 18 (10) (2021) 3843–3853.
[85] P.W. Hawkes, J.C. Spence, Science of Microscopy, vol. 1, Springer, New York, 2007.
[86] H. Le Ferrand, F. Bouville, T.P. Niebel, A.R. Studart, Magnetically assisted slip casting of bioinspired heterogeneous composites, Nat. Mater. 14 (11) (2015) 1172–1179.
[87] N. Saheb, U. Hayat, S.F. Hassan, Recent advances and future prospects in spark plasma sintered alumina hybrid nanocomposites, Nanomaterials 9 (11) (2019) 1607.
[88] P.F. Becher, M.V. Swain, Grain-size-dependent transformation behavior in polycrystalline tetragonal zirconia, J. Am. Ceram. Soc. 75 (3) (1992) 493–502.
[89] A. Heuer, N. Claussen, W. Kriven, M. Ruhle, Stability of tetragonal ZrO2 particles in ceramic matrices, J. Am. Ceram. Soc. 65 (12) (1982) 642–650.
[90] P.F. Becher, Toughening behavior in ceramics associated with the transformation of tetragonal ZrO2, Acta Metall. 34 (10) (1986) 1885–1891.
[91] U. Anselmi-Tamburini, J. Garay, Z.A. Munir, Fast low-temperature consolidation of bulk nanometric ceramic materials, Scr. Mater. 54 (5) (2006) 823–828.
[92] S.A. Cruz, R. Poyato, F.L. Cumbrera, J.A. Odriozola, Nanostructured spark plasma sintered Ce-TZP ceramics, J. Am. Ceram. Soc. 95 (3) (2012) 901–906.
[93] X. Chen, K. Khor, S. Chan, L. Yu, Preparation yttria-stabilized zirconia electrolyte by spark-plasma sintering, Mater. Sci. Eng.: A 341 (1–2) (2003) 43–48.
[94] F. Maglia, M. Dapiaggi, I. Tredici, B. Maroni, U. Anselmi-Tamburini, Synthesis of fully dense nanostabilized undoped tetragonal zirconia, J. Am. Ceram. Soc. 93 (7) (2010) 2092–2097.
[95] H. Zhang, Z. Li, B.-N. Kim, K. Morita, H. Yoshida, K. Hiraga, Y. Sakka, Highly infrared transparent nanometric tetragonal zirconia prepared by high-pressure spark plasma sintering, J. Am. Ceram. Soc. 94 (9) (2011) 2739–2741.
[96] K. Matsui, K. Hosoi, B. Feng, H. Yoshida, Y. Ikuhara, Ultrahigh toughness zirconia ceramics, Proc. Natl. Acad. Sci. 120 (27) (2023) e2304498120.
[97] S. Sarker, H.T. Mumu, M. Al-Amin, M.Z. Alam, M. Gafur, Impacts of inclusion of additives on physical, microstructural, and mechanical properties of alumina and zirconia toughened alumina (ZTA) ceramic composite, A Rev. Mater. Today: Proc. 62 (2022) 2892–2918.
[98] N. Mitra, S. Das, S. Maitra, U. Sengupta, A. Basumajumdar, Effect of CeO2 on the sintering behaviour of zirconia–alumina composite, Ceram. Int. 28 (8) (2002) 827–833.
[99] D. Ragurajan, M. Satgunam, M. Golieskardi, The effect of cerium oxide addition on the properties and behavior of Y-TZP, Int. Sch. Res. Not. 2014 (2014).
[100] K. Okada, T. Sakuma, The role of zener's pinning effect on the grain growth in Al2O3-ZrO2, J. Ceram. Soc. Japan 100 (1160) (1992) 382–386.
[101] T. Merle, R. Guinebretiere, A. Mirgorodsky, P. Quintard, Polarized raman spectra of tetragonal pure ZrO2 measured on epitaxial films, Phys. Rev. B 65 (14) (2002) 144302.
[102] B.-K. Kim, H.-o. Hamaguchi, Mode assignments of the raman spectrum of monoclinic zirconia by isotopic exchange technique, Phys. Status Solidi (B) 203 (2) (1997) 557–563.

[103] L.S. Dimas, M.J. Buehler, Tough and stiff composites with simple building blocks, J. Mater. Res. 28 (10) (2013) 1295–1303.
[104] R.H. Hannink, P.M. Kelly, B.C. Muddle, Transformation toughening in zirconia-containing ceramics, J. Am. Ceram. Soc. 83 (3) (2000) 461–487.
[105] J. Schlacher, T. Csanádi, M. Vojtko, R. Papšík, R. Bermejo, Micro-scale fracture toughness of textured alumina ceramics, J. Eur. Ceram. Soc. 43 (7) (2023) 2943–2950.
[106] A. Bravo-Leon, Y. Morikawa, M. Kawahara, M.J. Mayo, Fracture toughness of nanocrystalline tetragonal zirconia with low yttria content, Acta Mater. 50 (18) (2002) 4555–4562.
[107] M. Ruehle, N. Claussen, A.H. Heuer, Transformation and microcrack toughening as complementary processes in ZrO2-toughened Al2O3, J. Am. Ceram. Soc. 69 (3) (1986) 195–197.